ChemElectroChem

Research Article
doi.org/10.1002/celc.202300331

Chemistry Europe
European Chemical Societies Publishing

www.chemelectrochem.org

Special Collection

Photovoltaic Wafering Silicon Kerf Loss as Raw Material: Example of Negative Electrode for Lithium-Ion Battery**

Mads C. Heintz,[a] Jekabs Grins,[b] Aleksander Jaworski,[b] Gunnar Svensson,[b] Thomas Thersleff,[b] William R. Brant,[c] Rebecka Lindblad,[c, d] Andrew J. Naylor,[c] Kristina Edström,[c] and Guiomar Hernández*[c]

Silicon powder kerf loss from diamond wire sawing in the photovoltaic wafering industry is a highly appealing source material for use in lithium-ion battery negative electrodes. Here, it is demonstrated for the first time that the kerf particles from three independent sources contain ~50% amorphous silicon. The crystalline phase is in the shape of nano-scale crystalline inclusions in an amorphous matrix. From literature on wafering technology looking at wafer quality, the origin and mechanisms responsible for the amorphous content in the kerf loss powder are explained. In order to better understand for which applications the material could be a valuable raw material, the amorphicity and other relevant features are thoroughly investigated by a large amount of experimental methods. Furthermore, the kerf powder was crystallized and compared to the partly amorphous sample by operando X-ray powder diffraction experiments during battery cycling, demonstrating that the powders are relevant for further investigation and development for battery applications.

Introduction

In recent years, an increasing focus on circular economy, raw materials recycling, and sustainable consumption has emerged in Europe. The European Commission launched its "Circular Economy Action Plan" in 2015, and an updated version was adopted in 2020.[1,2] Among the key action points are ensuring less waste within sectors such as electronics and batteries. In this respect, industrial and commercial adaptation of silicon waste from the photovoltaic (PV) industry as a new raw material is of high relevance.[3] One such waste is the saw dust generated during wafering of solar cells by means of diamond wire sawing (DWS). In DWS, a prismatic silicon ingot is sawn into wafers by a long abrasive wire taking a single pass from the feed spool to the receiving spool. Approximately 40% of the silicon ingot is lost as a fine silicon powder due to the kerf of the wire.[4] This silicon powder kerf loss, hereafter *kerf*, is potentially a high-purity high-value raw material.

Previous reports on kerf recycling have largely focused on the re-introduction of the kerf to PV applications.[3–9] In general, this has proved costly, and compared to the extremely low cost of virgin solar-cell quality silicon, the methods are not commercially viable. This is due to inherent features of the kerf such as the small size of the particles, the oxidized particle surface, and the carbon and metallic contaminations. However, these features are not necessarily detrimental for use in other high value applications.

Silicon is seen as the holy grail for improving the anode in lithium-ion batteries (LIBs). The current development of LIB technology and the establishment of new production capacity is tremendous due to EU intending to ban fossil fuel cars by 2035.[10] Today, less than 10% of silicon in a carbon/graphite matrix is found in commercial LIBs[11] but if the content could increase, the overall energy content of the cell will grow by about 20%. The sources of silicon for batteries are in general expensive and with a large environmental footprint, as the purification processes are energy intensive. In 2017, the yearly global volume of generated Si kerf from the PV industry was 160000 tons,[9] and this amount is increasing proportionally with the rapidly increasing produced solar cell capacity. For comparison, 160000 tons is sufficient for the production of 2800 GWh of battery capacity at 20% Si and 3.5 V cell voltage. Access to low-cost, low-footprint, high-quality silicon such as kerf is highly

[a] Dr. M. C. Heintz
Resitec AS
Setesdalsveien 110, 4617 Kristiansand S (Norway)

[b] Dr. J. Grins, Dr. A. Jaworski, Prof. G. Svensson, Dr. T. Thersleff
Department of Materials and Environmental Chemistry,
Arrhenius Laboratory
Stockholm University
SE 10691 Stockholm (Sweden)

[c] Dr. W. R. Brant, Dr. R. Lindblad, Dr. A. J. Naylor, Prof. K. Edström, Dr. G. Hernández
Department of Chemistry,
Ångström Laboratory
Uppsala University
SE 751 21 Uppsala (Sweden)
E-mail: guiomar.hernandez@kemi.uu.se

[d] Dr. R. Lindblad
Department of Physics and Astronomy,
X-ray Photon Science
Uppsala University
SE 751 20 Uppsala (Sweden)

[**] A previous version of this manuscript has been deposited on a preprint server (DOI: https://doi.org/10.26434/chemrxiv-2023-fphj8)

Supporting information for this article is available on the WWW under https://doi.org/10.1002/celc.202300331

Special Collection This manuscript is part of a Special Collection on Electrochemical Interfaces in Energy Storage Devices.

appealing. The idea of applying kerf for use in Li-ion battery anodes is not novel,[12–16] but several fundamental features of the kerf has not yet been thoroughly treated in literature.

Earlier reports in literature have focused on the recovery of silicon from the waste slurry originating from abrasive SiC slurry wafering,[3,6] but DWS has since 2010 gradually become the preferred solution. As such, the features of the kerf and the challenges in recycling it have changed. Recently, efforts to recycle DWS kerf for use in PV,[5,9,17] production of bromosilanes,[7,8] and batteries[12–16] have been published. Vazquez-Pufleau et al. have described kerf properties and efforts to remove carbon impurities.[4,18] With a notable exception,[9] the papers in general do not examine the fundamental chemical and morphological properties of the kerf thoroughly.

In the present article, kerf from various sources in Europe and Asia are thoroughly characterized with the motivation of assessing their usefulness as LIB anode active materials. While the use in other technologies is not directly discussed in the text, the investigations are sufficiently thorough to serve as summary of general fundamental kerf properties regardless of the intended use case. The key properties investigated are the chemical contaminations, particle morphology, and degree of crystallinity. In addition, operando X-ray diffraction experiments are conducted as the first step for assessing their usefulness as an active anode material in lithium-ion batteries.

Results and Discussion

Bulk Chemical Composition

It is an ambition of this paper to provide insight into the properties of diamond wire sawing (DWS) kerf from the PV wafering industry as a general concept, in order to identify in which areas this class of material may be a suitable high-value raw material. To achieve this, samples from three different sources (named *kerf 1–3*) are analyzed and discussed in the context of the industrial processes. The composition of the ingot from which wafers are cut is of solar cell quality, which is typically more than 99.99% pure, containing primarily oxygen, carbon, and the intentional dopant elements.[19] Some commercial producers specify oxygen and carbon content to be <16 ppma (9.1 ppmw) and <2 ppma (0.86 ppmw), respectively.[20–22] Dopant concentrations are not disclosed by the manufacturers, but conductivity values are claimed to be 1–7 Ωcm for n-type, and 0.4–1.5 Ωcm for p-type. These conductivity values correspond to dopant levels on the order of 0.2–2 ppma.[23] Dopant elements are typically phosphorous for n-type and boron or gallium for p-type.[22–24] 2 ppma in a matrix of Si corresponds to 2.2 ppmw P, 0.77 ppmw B, and 5.0 ppmw Ga, as summarized in Table 1. This table contains experimental composition results from kerf 1–3, showing that P and B concentrations are within the expected range. The low Ga content suggests that these samples did not come from processes using Ga, but it is likely that future kerf sources will contain more Ga and less B. The kerf is not exposed to conditions allowing for diffusion, meaning that any impurities deviating from wafer specifications should be located on the kerf particle surfaces or as separate particles.

External impurities may originate from the cutting fluid, the diamond wire, or the glue and beam. The beam is a sacrificial material onto which the ingot is attached so that the cut can extend all the way through the ingot without cutting into the machinery. The composition of the beam varies between producers, but the source of kerf 1 supplied a sample. This material consisted of 60% $Al(OH)_3$ in a matrix of poly(methyl methacrylate) (PMMA). Extrapolating the 0.7% Al concentration in kerf 1 obtained by X-ray fluorescence spectroscopy (XRF) in Table 1 implies that the beam contributed to 0.8% C and 1.7% O. This corresponds to 1.3% PMMA and 2.0% $Al(OH)_3$, and the potential of 0.7% H_2O should $Al(OH)_3$ decompose to Al_2O_3 and water. The low concentrations of Al in kerf 2 and 3 suggest that these producers use a different beam material.

The cutting fluid is most commonly water with various additions. These additives are continuously improved, and different manufacturers use different confidential formulations, likely containing organic molecules such as tensides and other surfactants.[25–28] The products are typically added as 1–2% in water, translating to 1–2% relative to dry kerf filter cake if the cake contained 50% moisture and the additives did not

Table 1. Bulk composition concentrations. Unmarked values are from glow discharge mass spectrometry (GDMS). All values are in ppmw unless marked by %. The columns noted *Kerf 1–3* are actual analysis results, while other columns are estimates from the discussion included for convenience. The complete GDMS analysis results are shown in Table SI 1.

Conc. (ppmw)	Kerf 1	Kerf 2	Kerf 3	Common PV level	Kerf 1 beam (rel. 0.7% Al)	Kerf 1 coolant and oxide est.
O[a]	3.5%	5.0%	5.0%		1.7%	1.8%
C[a]	2.5%	1.0%	2.0%		0.8%	1.7%
P	2.8	4.0	1.0	2.2		
B	0.25	1.8	0.42	0.77		
Ga	0.21	0.19	0.03	5.0		
Al	0.7%[b]	490	20		0.7%	
Ni	54	180	200			
Fe	2.9	610	10			

[a] LECO, [b] X-ray fluorescence spectroscopy (XRF)

evaporate during drying. In addition to the additives, salts and other impurities originating from the process water will also be present in the kerf. Assuming that most of the carbon contamination in kerf 1 comes from the beam and the cutting fluid, it implies that the cutting fluid has contributed to ~1.7% C, which corresponds well to the estimate above. Similarly, 1.8% oxygen originates from cutting fluid and surface oxide layer combined.

The diamond wire is reported to be a ~60 μm thick high carbon steel with diamonds of 8–20 μm embedded in a layer of electroplated nickel.[29] This is confirmed by light microscopy images (Figure SI 1) of unused and spent wire supplied by the kerf 1 wafer manufacturer. There is no appreciable reduction in wire thickness for the used wire, indicating that nickel or steel contamination should be minor. It is clear, however, that the diamonds have decreased significantly in size, as they protrude further from the wire surface on the unused wire. We have not found any indications of discernable diamond contamination in the kerf. Trace metal analysis by glow discharge mass spectrometry (GDMS) shown in Table 1 confirm that Ni and Fe contamination in general is low, but Ni contamination from the wire surface is detected at 50–200 ppmw, while Fe is essentially absent for kerf 1 and 3. Kerf 2, on the other hand, contained 610 ppmw Fe, which could be indicative of the use of a lower quality wire, or a wire that had been used beyond its service life. It is noted that the Fe contamination could be partially explained by other causes, such as process water contamination. Interestingly, kerf 2 additionally contained elevated values of common steel alloying elements such as Mn, Cr, V and Mo, as seen in the complete chemical analysis in Table SI 1.

Surface Composition and Separate Particles

The surface composition of the samples was analyzed by X-ray photoelectron spectroscopy (XPS), and a summary of the results are presented in Table 2, while the detailed results and refinements may be found in Figure SI 2. The carbon environments are similar for all samples, with mostly C–C and C···O environments present. O 1s spectra are consistent with the presence of SiO_x environments, with one peak fitted for such species. However, a broadening at lower binding energies for kerf 1 indicates the presence of another oxygen species, likely to be $Al(OH)_3$ as supported by the refined Al to O ratio. Si 2p spectra indicate the presence of elemental silicon as well as SiO_x, mostly in the form SiO_2.

Also presented in the table is the ratio of Si in oxide form to elemental Si, which serves as a qualitative indication of oxide layer thickness due to the shallow penetration depth of XPS signals. Further presented in the table are estimated values for O contained in organic molecules, obtained by multiplying the C LECO bulk concentration (Table 1) with the fraction of C

Table 2. Surface and structure properties of kerf.

Property	Kerf 1	Kerf 2	Kerf 3
Summary of characterizations			
d_{50} (laser diffraction)	1.0 μm	0.8 μm	1.0 μm
SSA (BET)	21.1 m^2/g	25.8 m^2/g	20.8 m^2/g
Amorphous fraction (XPRD)	50%	49%	46%
Amorphous fraction (Raman)	53%	50%	53%
XPS surface composition (at%)			
Elemental Si	30.9	26.4	27.6
Si as SiO_2	16.3	23.5	20.5
O as SiO_2	27.1	41.9	36.9
$Si^{+1}/Si^{2+}/Si^{3+}$	3.5	3.3	3.3
Total C	14.4	4.9	11.7
C bound to O (C–O/C=O/O=C–O/CO_3^{2-})	4.5	1.5	4.1
Al as $Al(OH)_3$	2.1	0	0
O as $Al(OH)_3$	5.6	0	0
Estimations			
SSA (laser diffraction)[a]	3.2 m^2/g	4.0 m^2/g	3.4 m^2/g
$Si_{oxide}/Si_{elemental}$ ratio (XPS)	0.53	0.89	0.74
O as C···O rel. total C_{XPS} (at%)[a]	5.2	1.7	4.7
wt%O/wt%C (XPS)[a]	0.48	0.46	0.54
O as C···O rel. dry kerf bulk (wt%)[a]	1.2	0.46	1.1
wt%O as oxide bulk[a]	1.1	4.5	3.9
Estimated oxide thickness[a]	0.36 nm	1.3 nm	1.4 nm

[a] Estimations for arguments sake. These values are calculated with the intention of disproving the assumptions on which they were made. The values must not be read literally.

bonded to O (relative to total C) according to XPS. This value was further used to estimate the oxide layer thickness accounting for measured specific surface area (SSA) and the deduced $Al(OH)_3$ content of kerf 1. The calculation method is described in the Supporting Information, and the resultant relationship between SSA, oxygen content as surface oxide, and oxide layer thickness is illustrated in Figure SI 3. While the general trend of thinner layer for kerf 1 compared to kerf 2–3 results for both methods of estimation, there remains a significant discrepancy in the amount of estimated oxide. If the estimated thickness values were correct, a significantly higher $Si_{oxide}/Si_{elemental}$ ratio would be expected for kerf 2–3. This suggests that the assumption that all oxygen according to LECO is in the form of surface bound oxide is faulty, and that there must another source of O in kerf 2–3 which is not surface bound.

The compositions of the beams used for kerf 2 and 3 are not known, but the low C and metallic contamination levels could be explained by the use of a silicon-based material such as glass (SiO_2) or silicon metal. Use of a glass beam would explain the relatively low SiO_2 XPS signal discussed in the previous paragraph, as separate glass particles would contribute more to LECO bulk concentration values, while a surface oxide would contribute more to XPS surface signal. Glass was common during SiC slurry cutting, and might still be a common beam material. Beams of graphite have also been reported.[13] A polymer-based material is unlikely for kerf 2, since the carbon content must also be partially attributed to cutting fluid. For kerf 3, the carbon content is high enough to conceivably be a combination of low concentration cutting fluid additive with only a shallow cut into a carbon-based beam.

Particle Morphology

The laser diffraction particle size distribution (PSD) results are shown in Figure SI 4. It can be seen that the measured particle sizes range from 200 nm to 10 μm. The mean particle size, d_{50}, was 1.0 μm for kerf 1 and 3, and 0.8 μm for kerf 2. Assuming spherical particles gives specific surface area (SSA) values which are ~6 times less than the BET SSA results, both provided in Table 2. This suggests that the morphology of the particles is anisotropic (not spherical) and/or that the powders are agglomerated or porous.

Scanning electron microscopy (SEM) image of kerf 1 presented in Figure 1 and of kerf 2–3 in Figure SI 5 show that the visual morphology of the particles is highly anisotropic. All samples demonstrate flakes of various sizes, ranging from less than 100 nm to a few μm in length. It appears that no particles are thicker than ~200 nm. The flake-like morphology is consistent with the discrepancy in laser diffraction and BET results. It is readily apparent from SEM images that the surface area is much greater than what would be the case for spherical particles of approximately 1 μm size. For powders of this type, laser scattering PSD results should be treated with caution, as the method is evidently not well suited to capture the features of this morphology.

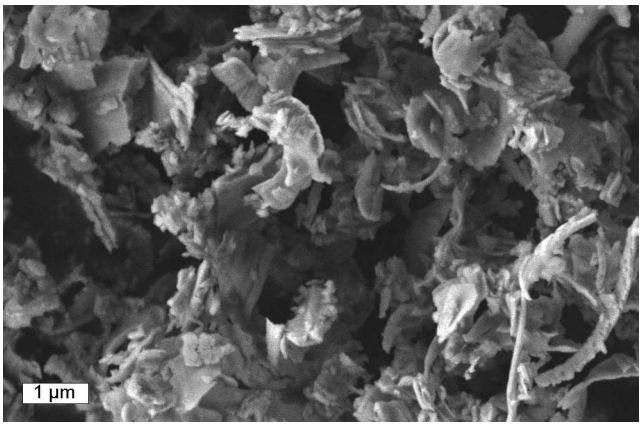

Figure 1. SEM image of the kerf 1 sample. Images of kerf 2–3 are shown in Figure SI 5.

Crystallinity of the Powders

According to what has been reported in literature, kerf silicon is crystalline. However, the X-ray powder diffraction (XRPD) patterns recorded here and presented in Figure SI 6 suggest otherwise. The diffractograms were essentially identical for the samples, and an appreciable amount of amorphous silicon (Si-a) was detected. The amorphous signal is seen as a broad intensity distribution at ~52°,[30] between the 220 and 311 stable crystalline polymorph (Si-I) peaks. Si-a also has a broad peak at ~28.3°, which is harder to observe here as it lies at the same position as the 111 Si-I peak. The kerf samples are qualitatively very similar to each other, clearly deviating from the crystalline reference (Figure SI 6). For the kerf, the peak shapes are near to hypo-Lorentzian, which is typical for broad log-normal grain size distributions.[31]

As a measure of the fraction of Si-a, the integrated intensity of the Si-a intensity maxima was compared to that of the sum of the integrated intensities of the Si-I 220 and 311 peaks. An example of a fit is shown in Figure 2a for kerf 1. A Gaussian peak shape was assumed for Si-a and a pseudo-Voigt peak shape for Si-I. The background was estimated by a linear interpolation between two points outside the peak region. Peak fits were made using both Panalyticals software HighScore + and the Fityk software,[32] yielding practically identical results. The determined phase fractions of Si-a for the different kerf samples were 46–50 %, summarized in Table 2. Despite the clear differences in the patterns and the appreciable amount of Si-a, this phase has been overlooked in literature (see below).

The Raman experiments presented in Figure SI 7 were carried out to further investigate the crystallinity of kerf 1. Crystalline silicon gives a peak at 532 cm^{-1} while the broad band centered at 480 cm^{-1} corresponds to amorphous silicon.[33,34] The samples were found to be stable under irradiation of a laser power of 0.5 mW, but to crystallize under higher powers. The fraction of amorphous silicon was determined from the relative intensities of the amorphous and crystalline components (assuming the Raman cross sections for Si-a and Si-I are equal).[35] The amorphous band was assumed to

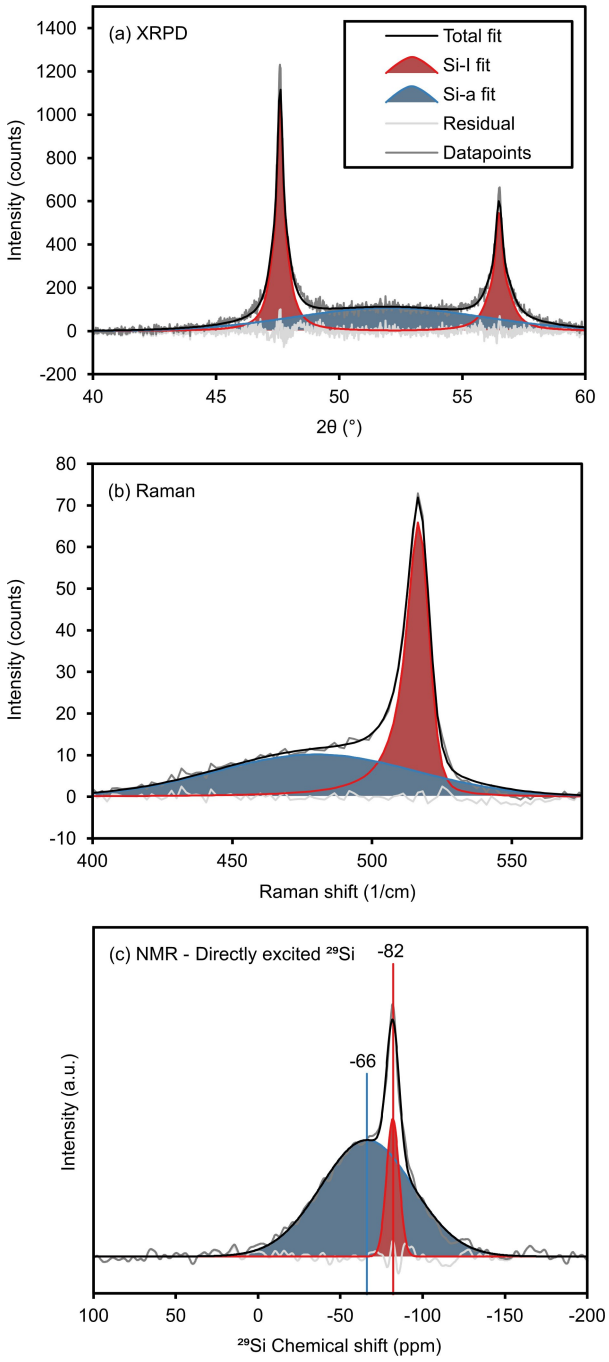

Figure 2. (a) A fit of a part of the XRPD pattern of kerf 1 to extract the fraction of Si-a relative to crystalline silicon (Si-I). The maximum peak intensity is ~5000 counts. (b) Fit of the Raman spectra for kerf 1 with a split pseudo-Voigt crystalline peak and a broad Gaussian amorphous peak. The corresponding fraction of Si-a is accordingly 53 %. (c) ^{29}Si MAS NMR spectrum for kerf 1, showing deconvoluted signals of amorphous and crystalline phases.

have a Gaussian shape. The crystalline peak was found to be slightly asymmetric, with a tail towards a lower wave-number. It was therefore fitted using a split pseudo-Voigt function. The fitting was made using the Fityk software.[32] The fit for kerf 1 is shown in Figure 2b. The determined amorphous fractions are between 50 and 53 % (see Table 2), in agreement with XRPD results.

^{29}Si magic-angle spinning (MAS) nuclear magnetic resonance (NMR) spectra were recorded to further confirm the coexistence of amorphous and crystalline silicon phases in the sample, shown for kerf 1 in Figure 2c. Two overlapping resonances are discernible, the broad one centered at −66 ppm, and the narrower one at −82 ppm. These are assigned to Si-a and Si-I, respectively. To corroborate the phase assignments, the silicon 640d XRPD reference was analyzed for comparison (see Figure SI 8a). The reference showed sharp resonance with chemical shift of −82 ppm, identical to that of the narrow signal component observed for the kerf sample. Moreover, ^{1}H-^{29}Si cross-polarization (CPMAS) spectrum of the kerf specimen was recorded (Figure SI 8b), and no signal corresponding to that of the amorphous silicon was found, despite weak signals in the range from −80 to −104 ppm, which can be assigned to minute amounts of surface silanol and siloxane moieties.[36–38] These results indicate that there is no hydrogen (or internal hydroxyls) in the Si-a, and that the broad signal at −66 ppm indeed corresponds to the interior of the particles and not the amorphous species present at the particle surface. Broad ^{29}Si signals with NMR shifts of −60 and −65 ppm were observed previously in ^{1}H-^{29}Si CPMAS NMR spectra of amorphous hydrogenated silicon films.[39,40] Recently, similar (although very weak) amorphous silicon signal component was observed at approximately −75 ppm in the pristine semicrystalline Si material, and between −60 and −85 ppm for the delithiated silicon in the cycled pouch cells.[41] Note that due to the very long relaxation times of crystalline silicon, the spectrum of Figure 2c is not quantitative; the integral of the signal of amorphous silicon is expected to be significantly overrepresented.

An additional remark could be made on the structure of the amorphous content. The relatively small difference in shifts between Si-I and Si-a in NMR and Raman means that the bond strengths are relatively similar, suggesting that the structures are not that different on a short length scale.[42–44] In fact, the quantitative validity of the refinement phase ratio calculations relies on this fact.

To the best of our knowledge, the amorphicity of kerf has not yet been reported. A few papers report on kerf from the DWS process. Vazquez-Pufleau et al. thoroughly analyzed a similar kerf by means of TEM and XRPD, and identified that the particles were not monocrystalline.[18] They argued that the particles were polycrystalline, but their XRPD pattern seems like it might contain the same amorphous signal seen here. Kasukabe et al. did not identify any amorphous content, but the XRPD results presented seem to contain the same amorphous signal ~52°.[13] Several authors present kerf treatment processes containing temperature treatments where the amorphous content could have crystallized. In all cases, however, the XRPD analysis of the pre-treatment sample might contain the amorphous signal.[8,14,16] Other articles treating the recycling of kerf from the DWS process did not consider crystallinity or conduct relevant analysis techniques (prior to significant material processing).[4,5,7,9,17]

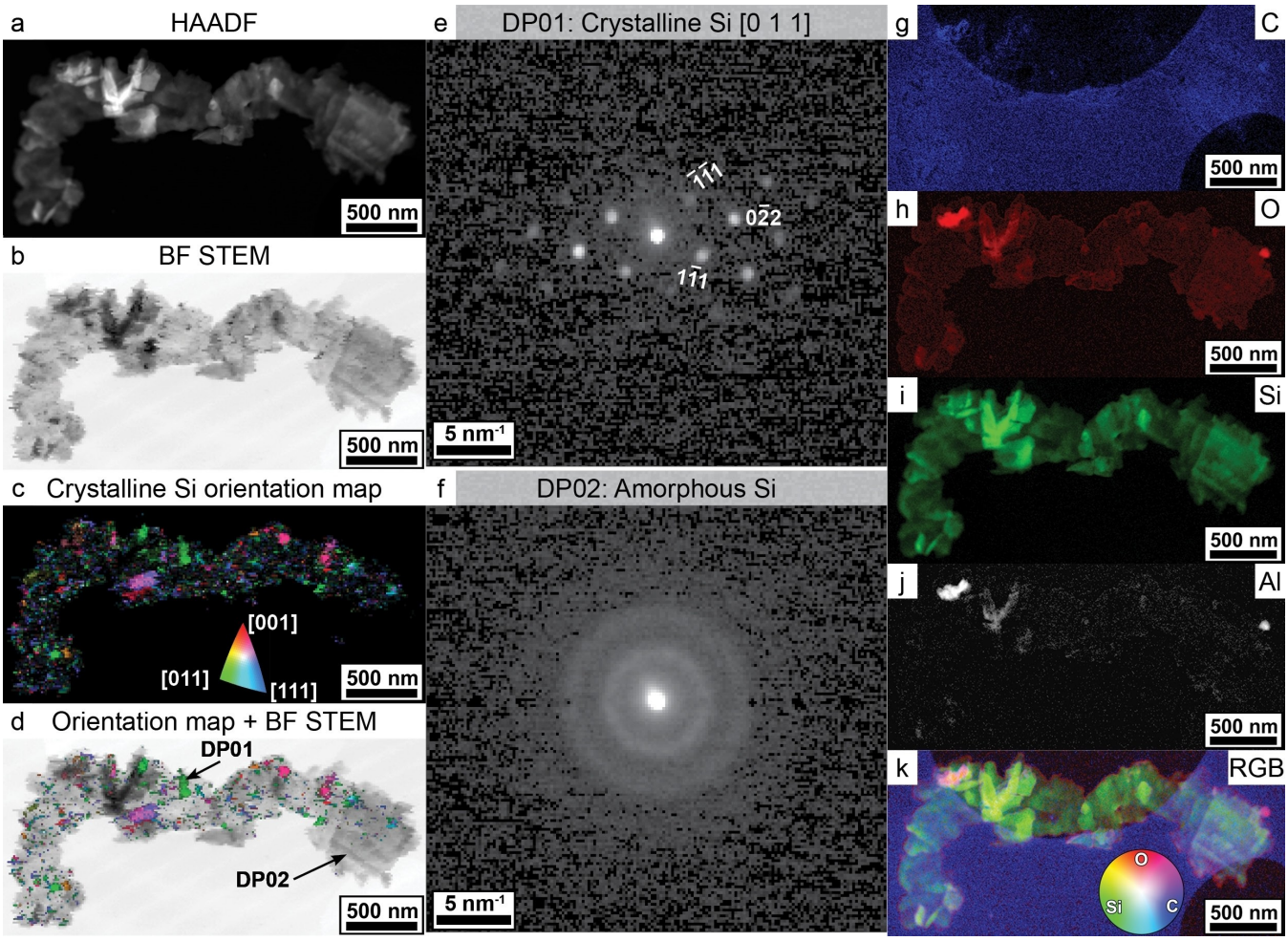

Figure 3. Scanning transmission electron microscopy (STEM) investigation of kerf 1. (a) High angle annular dark field (HAADF) image. (b) Bright field (BF). (c) crystallite orientation map generated from virtual dark field images, and (d) the same map superimposed on the BF image. (e,f) Diffraction patterns obtained by placing the aperture at the locations marked in (d). (g–k) Energy dispersive x-ray spectroscopy (EDX) maps.

Origin of the Amorphous Phase Content

When considering that PV silicon is, by design, the stable polymorph Si-I, the amorphous content may initially be counter intuitive. The same can be said for the thin shavings observed by SEM, as Si-I is brittle, and brittle mode fracture surfaces are typically faceted. As will be discussed, however, the observed crystallinity and morphology could in fact be expected due to the nature of the DWS wafering process.

The wafering process has been extensively studied and developed over several years and technology iterations.[29,45,46] Ingots from which the wafers are cut are of the stable diamond cubic silicon polymorph (Si-I). However, the wafering process is designed such that the pressure exerted on the silicon from the diamond wire causes a phase transition to the ductile metallic Si-II polymorph, yielding fewer cracks and wafer surfaces of higher quality than what would be the case for abrasion of the brittle Si-I.[29] The resulting phase composition on the surface of the wafers has been extensively studied dating back several decades.[47–51] Upon exposing silicon to hydrostatic pressure, the ductile metallic Si-II is formed at 10-13 GPa, and rapid unloading from 4 GPa results in amorphous silicon (Si-a). Because the presence of amorphous silicon on the wafer surfaces is so well known, it is surprising that its presence in the kerf powder has not yet been identified.

Lending experience from the wafer optimization literature, Si-III, Si-XII, and Si-IV could be expected in addition to Si-I and Si-a in the kerf. An XRPD pattern of kerf 1 was recorded for a prolonged time in order to find possible evidence for other metastable silicon polymorphs (figure not included). Two very weak peaks could be observed at positions corresponding to the strongest peaks of Si-III.[52] If the signature originates from Si-III, the amount is estimated as 1–2% of the total crystalline silicon content. In other words, we find that the concentration of other polymorphs (than Si-I and Si-a) is none or negligible. Gassilloud et al. found that slow speed nanoscratching of silicon led to metastable Si-XII, while faster speeds led to Si-I and Si-a only due to the fast pressure release.[50] The wire speeds used in DWS is even faster by 5 orders of magnitude, supporting our findings that only Si-I and Si-a are present. For detailed information on the phase evolutions in the DWS process, the reader is referred to the literature.[50,53]

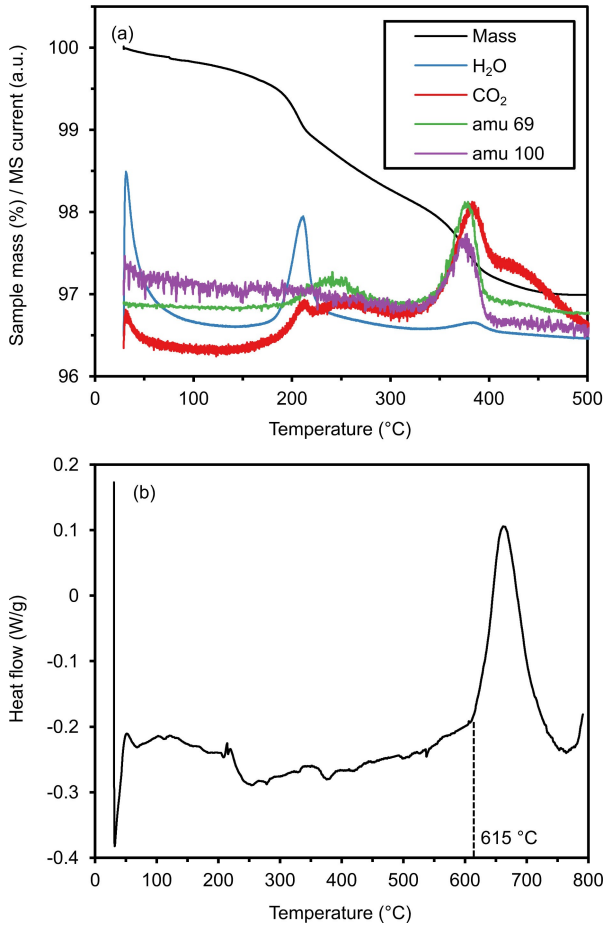

Figure 4. (a) TG-MS curves for kerf 1 heated in Ar atmosphere with 10 °C/min. The curves for amu 69 and amu 100 are smoothed. (b) DSC curve for kerf 1 upon heating in Ar atmosphere at 10 °C/min up to 800 °C.

Internal Particle Morphology

Investigation of a sample of kerf 1 by scanning transmission electron microscopy (STEM) is presented in Figure 3. High angle annular dark field (HAADF) and bright field (BF) overview images are shown in Figure 3a,b. The 4D STEM datacube employed allows for the generation of virtual dark field images, performed by using annular circular detectors centered on the expected location of the Si-I 311 and 111 lattice planes. All of the diffraction patterns were indexed to Si-I using the automated orientation mapping function in the py4DSTEM software package.[54] The orientations are mapped to false colors and superimposed over the BF image in Figure 3d. The crystallites within the amorphous matrix of the particle are unevenly distributed, and regions of the particle are purely amorphous, suggesting that the presence of crystallites may be dependent on aspects such as closeness to diamond contact, depth of scratch or similar. Diffraction patterns at two locations marked in Figure 3d are presented in Figure 3e,f, confirming that these regions are indeed crystalline and amorphous, respectively.

Composition of the microparticle was investigated using electron energy-loss spectroscopy (EELS) and energy dispersive X-ray spectroscopy (EDX). These datasets were combined using hypermodal data fusion (HyDF)[55,56] and the elemental maps in Figure 3g–k were extracted from the resulting EDX model. Only four elements were observed: C, O, Al, and Si. The C map reveals the support layer as well as a small contribution from carbon, presumably sitting on the surface of the microparticle. The Si map reveals that the microparticle consists primarily of elemental Si. The O map reveals that O is also present in this microparticle. However, it is largely concentrated around the edges, strongly suggesting that it constitutes an encapsulating layer. Finally, a limited area shows signal of Al. This is assigned to an $Al(OH)_3$ particle sitting on the surface, supported by the strong O signal from the same region coupled with the known $Al(OH)_3$ content of the beam.

Thermal Analysis

Thermogravimetric and gas mass spectrometry analysis (TG-MS) curves for heating kerf 1 in Ar atmosphere are shown in Figure 4a. Up to ~400 °C, the sample loses about 3% of the weight in two steps. TG curves for runs in air and inert atmospheres were found to be very similar. The step at ~200 °C is due to decomposition of $Al(OH)_3$ to Al_2O_3 and H_2O. As discussed above and summarized in Table 1, this decomposition is expected to cause a mass loss of 0.7% relative to dry kerf mass, and it is well known to decompose at just above 200 °C. The MS curves confirm that this first step is mainly associated with loss of water. The second step is attributable to the decomposition of poly(methyl methacrylate) (PMMA),[57,58] which is also a significant contamination from the beam. The atomic mass units of both 100 and 69 originate from PMMA, corresponding to the monomer (methyl methacrylate) and a monomer fraction, respectively.

Thermogravimetric differential scanning calorimetry (TG-DSC) curves recorded in N_2 atmosphere with the Netzsch Jupiter STA (figure not included) showed no weight change in the region 400–1100 °C. A small reproducible exothermal peak was observed at ~640 °C due to the crystallization of Si-a. For a better characterization of this peak, a DSC curve between 25 and 800 °C in Ar atmosphere was measured with a sensitive Setaram SENSYS Evo. Figure 4b shows the result. The onset of the crystallization was 615 °C and the transition enthalpy 104.73 J/g (relative to total sample). Crystallization of amorphous silicon thin films has been extensively studied for solar cell applications, and crystallization at ~600 °C is comparable to literature values.[59] Because the amorphous content of the sample was only ~50%, the crystallization enthalpy corresponds well to literature values in the range 200–450 J/g (relative to 100% Si-a).[60]

Figure 5 shows the result of STEM investigation of a sample heat treated at 550 °C in N_2, demonstrating that the particle morphology was not significantly affected at this temperature. The HAADF survey images (Figure 5a,b) reveals that the qualitative morphology of the particles did not change relative to the sample that was not heat treated (Figure 3). The low-angle ADF and bright field STEM images (Figure 5b) reveal

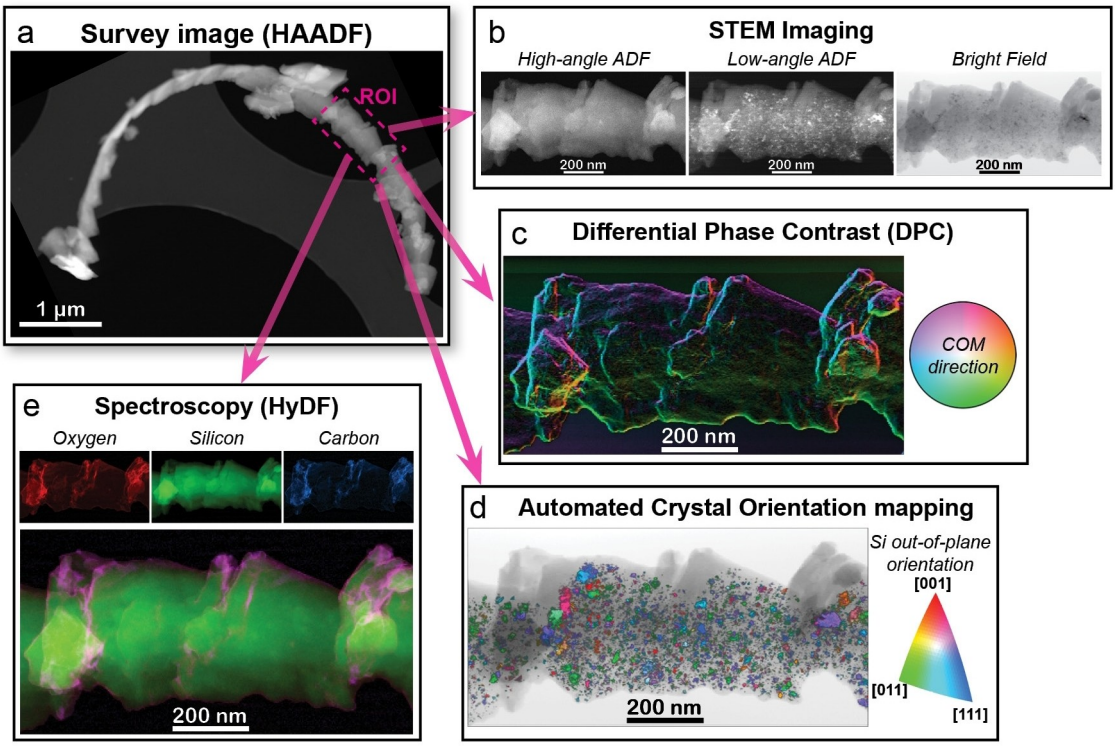

Figure 5. Scanning transmission electron microscopy (STEM) investigation of kerf 1 heat treated at 550 °C in N_2.

contrast consistent with the presence of small crystalline nanoparticles with a typical size less than 20 nm embedded within an amorphous matrix. This is confirmed through use of 4D-STEM scanning diffraction on the region of interest (ROI). As with the non-heat treated particle (Figure 3), all of the individual diffraction patterns were indexed as crystalline Si-I using the Automated Crystal Orientation mapping feature of the py4DSTEM software package[54] and their orientations were mapped to false colors and superimposed over the bright-field STEM image in Figure 5d. It is immediately evident that the nanoparticles are randomly oriented and cluster within the lower regions of this ROI. The composition of the ROI (Figure 5e) was determined using HyDF,[55,56] revealing that the entire agglomerate is Si-rich. The upper regions of the ROI that do not contain crystalline Si are nevertheless Si-rich and, thus, are primarily amorphous Si. Additionally, a thin SiO_2 layer is observed on the surface along with C contamination. The differential phase contrast (DPC) image (Figure 5c) was generated by tracking translations of the center of mass (COM) of the central diffraction disk and is very sensitive to small changes in sample thickness. This therefore maps out the surface morphology of the sample in great detail.

Electrochemical Behavior

While kerf has already been reported as an anode material for lithium-ion batteries,[13,14,16] it has been considered a crystalline material, contrary to what has been demonstrated above. Therefore, herein we investigate the electrochemical behavior of the partly amorphous kerf 1 and compare it to its crystalline analogous (kerf 1-850). The latter was obtained by heat treating kerf 1 in air to 400 °C to remove organic impurities, and to 850 °C in argon to crystallize the particles.

The voltage profiles of the first lithiation and delithiation can be found in Figure 6a. Kerf 1 shows two characteristic plateaus, the first one at around 0.17 V vs. Li^+/Li until 1000 mAh/g and the second one at around 0.08 V vs. Li^+/Li with a sloping profile until the potential drops to the cut-off voltage at 0.01 V vs. Li^+/Li. A final lithiation capacity of 3400 mAh/g is obtained after the constant voltage step. The upper plateau has been previously assigned to the lithiation of amorphous silicon phase and the latter of crystalline silicon.[61] This can be confirmed when compared to the fully crystalline sample (kerf 1-850) that only features the bottom plateau at around 0.08 V vs. Li^+/Li, reaching a capacity of 4400 mAh/g after the constant voltage step. The experimental capacity exceeds the theoretical which could be due to the SEI formation and side reactions known to occur with silicon electrodes. The coulombic efficiency for both samples is 81 % which suggests that the reversibility of the lithiation/delithiation processes in the first cycle is barely affected by the degree of crystallinity of the sample.

This difference in the lithiation profiles of the partly amorphous and fully crystalline kerf has been further investigated with operando XRPD measurements presented in Figure 6b,c. In order to get strong XRPD signals, the electrodes were prepared with higher active mass loading of around 5 mg/cm^2 (compared to 1.2 mg/cm^2 in the previous experiments) and without stack pressure. Unfortunately, this comes at a cost in

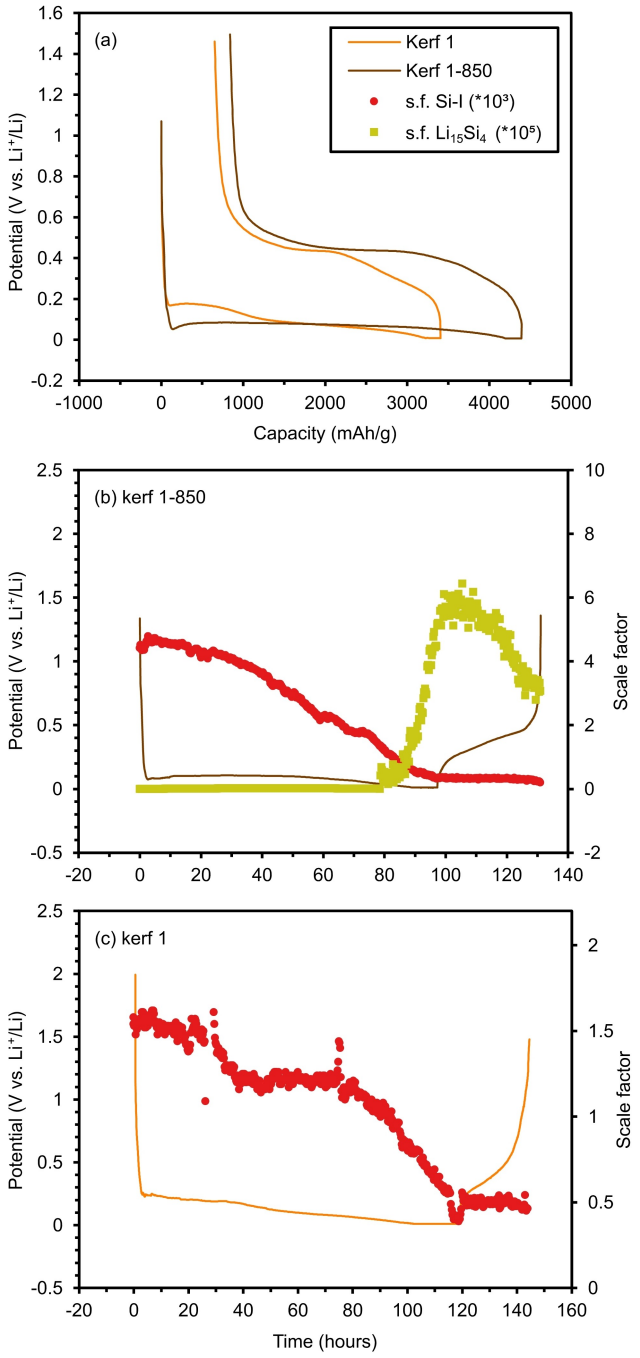

Figure 6. (a) First lithiation/delithiation profile of partly amorphous kerf (kerf 1) and crystallized kerf (kerf 1-850). (b) Si-I and $Li_{15}Si_4$ scale factors (s.f.) from operando XRPD of high mass loading electrodes for kerf 1-850 cycled at C/100. (c) Si-I scale factor from operando XRPD of high mass loading electrodes for kerf 1 cycled at C/150.

the electrochemical performance with higher cell resistance and lower coulombic efficiency. Therefore, low C-rates are preferred for in-house experiments. Nevertheless, the voltage profiles of both samples are similar to the cells with lower active mass loading, with two plateaus for the partially amorphous kerf 1 and one plateau at lower voltage for the crystalline sample kerf 1-850. However, the lithiation capacity is different, reaching 3395 mAh/g and 2540 mAh/g for crystallized and partially amorphous samples, respectively. The theoretical capacity of silicon is 3579 mAh/g, and the discrepancy could be explained by the poor electrochemical setup used for this experiment, where obtaining strong XRPD signals was prioritized.

The initial diffractogram shown in Figure SI 9 features the peaks from Si-I at 28.6° and 47.5°, as well as peaks from the other cell components. Here, we will only focus on the evolution of the scale factor, which is proportional to the amount of each phase (Si-I and $Li_{15}Si_4$). Figure 6b shows the results from the crystalline kerf 1-850. The scale factor of Si-I decreases continuously as the lithiation occurs, but it does not disappear completely when lithiation finishes. Instead, 7.3 % Si-I remains unlithiated which is close to the capacity left (5.2 %) to reach silicon's theoretical capacity for $Li_{15}Si_4$ (3579 mAh/g). The growth of $Li_{15}Si_4$ starts when the voltage goes below 0.04 V vs. Li^+/Li and capacity reaches ~2800 mAh/g and continues to grow until the end of the lithiation step, reaching a capacity of 3395 mAh/g. During the delithiation, the scale factor of Si-I remains constant while for $Li_{15}Si_4$ it decreases although not completely. This indicates that the sample does not fully delithiate under the experimental conditions and contributes to the low coulombic efficiency observed for this cell (35.5 %).

Figure 6c shows that the phase evolution of the partially amorphous sample is different from the fully crystalline sample. The scale factor of Si-I remains constant until the voltage reaches 0.2 V vs. Li^+/Li and the capacity reaches ~650 mAh/g. This confirms the previous results and the suggestions in literature that the amorphous silicon phase lithiates first.[62–64] With further lithiation, there is a slight decrease in the scale factor of Si-I before it again remains constant while amorphous silicon is lithiated. From 0.07 V vs. Li^+/Li and capacity ~1800 mAh/g, the most significant decrease in Si-I scale factor occurs, although 0 is still not reached for this sample either. The remaining 35 % Si-I scale factor corresponds well with the 29 % remaining capacity to reach the full theoretical capacity for $Li_{15}Si_4$. Interestingly, the formation of crystalline $Li_{15}Si_4$ was not observed in XRPD throughout the whole experiment, even though the voltage was held at 10 mV vs. Li^+/Li until the current dropped to C/250 (Figure SI 10). This is suggested to be explained by the low degree of lithiation ($Li_{2.6}Si$, instead of $Li_{3.75}Si$) rather than the presence of the amorphous phase initially.

To investigate the lithiation and phase development toward the fully lithiated state, additional in situ experiments were carried out until full theoretical capacity was achieved (3579 mAh/g) with stack pressure to improve the electrochemical response. Figure SI 11 shows that the peak from Si-I, at ~28.4°, has disappeared completely for both kerf 1 and kerf 1-850 when fully lithiated. This confirms that the unreacted crystalline silicon from the operando experiments remained because the full theoretical lithiation capacity had not yet been reached at the sub-optimal cycling conditions. Furthermore, both samples showed the formation of crystalline $Li_{15}Si_4$, with peaks at ~20.2°, ~23.4°, and ~26.2°, at the fully lithiated state (Figure SI 11), suggesting that the reason why this phase was not seen with the partially amorphous sample during operando experiments was due to the low lithiation degree achieved.

Upon delithiation, the peak from crystalline $Li_{15}Si_4$ disappeared almost completely in kerf 1-850 and small amounts remained for kerf 1. Neither kerf 1 nor kerf 1-850 reestablished the Si-I phase, evident by the lack of peaks arising in the XRPD patterns (Figure SI 11). The fact that the coulombic efficiency is still low in both samples, 40% for kerf 1-850 and 27% for kerf 1, compared to the high values obtained with lower mass loading (81%), suggests that the Li_xSi phase remains after delithiation.[65]

Overall, the obtained electrochemical results further confirm the presence of amorphous silicon in the kerf, as seen in the upper plateau at around 0.2 V vs. Li^+/Li. This indicates that electrochemistry is another technique to characterize this type of material and to differentiate it from a fully crystalline sample. As previously mentioned, kerf has already been reported as an anode material, however, the presence and effect of the amorphous part has been overlooked. In many of the papers they show the two similar plateaus during lithiation as we found for the partly amorphous kerf and the broad intensity distribution at ~52° in their XRPD patterns. This suggests the presence of amorphous phase in their samples even if this has not been mentioned.[13,14] From our results, we can conclude that regardless of the initial degree of crystallinity, both samples undergo similar phase transitions during lithiation and delithiation. Furthermore, with optimized electrochemical setup a high initial capacity and coulombic efficiency are achieved for the kerf as-is (kerf 1) and the crystalline heat-treated kerf (kerf 1-850) which strengthens the appeal of further developing anode silicon from the kerf family of silicon powders.

Conclusions

Kerf samples from 3 different sources were thoroughly characterized based on their physical and chemical properties. Contrary to what has been previously reported, the kerf is shown to contain ~50% amorphous silicon for all sources. A few articles have done similar investigations previously, but they focused on preparing a solar-grade feedstock, and neither reported the presence of amorphous silicon or the particle internal morphology.[4,9,18] In the present work, the particles were further characterized and shown to consist of an amorphous matrix with embedded crystallites on the order of 10 nm in size. Similar to other reports, the particles were found to be flake-like in morphology with thickness of less than 200 nm and length of up to a few μm. The specific surface area was 20–25 m^2/g. The surface oxide layer was found to be less than 1 nm for all samples. The amorphous content was shown to be elemental and in the bulk of the particles (as opposed to some surface feature), by NMR and STEM. Chemical contamination of the kerf samples varied between sources, as expected, due to differences in process parameters such as cooling fluid composition, beam material and wire quality. These differences are not given much focus here, as their exact features are bound to change between sources and even over time for a single source as their process changes. In general, beam and cutting fluid are most significant, contributing to ~1–2% each relative to dry kerf mass. Metallic impurities are generally below 100 ppm, with nickel from the electroplated wire being the most certain influence.

A selected sample was characterized during heat treatment, demonstrating that impurity decomposition happens as expected. More significantly, the crystallization of the amorphous phase was identified to initiate at ~615 °C at 10 °C/min ramp rate. The associated crystallization enthalpy was 104.73 J/g for a sample containing 50% amorphous phase. No qualitative difference in the particle morphology was observed after annealing at 550 °C, still containing small crystallites within an amorphous matrix, while samples heated to 850 °C were shown by XRPD to be completely crystalline.

The partly amorphous sample was compared to a crystallized sample by operando and in situ XRPD cycling experiments. A higher voltage plateau corresponded to the lithiation of the amorphous phase of the partly amorphous sample, while the lower plateau (also present in the crystallized sample) corresponded to the crystalline silicon. Although this behavior of kerf can be seen in published results, the authors nonetheless considered their material as crystalline. While both samples studied here showed similar initial capacity and coulombic efficiency, further studies are required to investigate its effect on the long-term cycling performance. Overall, this paper shows the potential application of the silicon kerf in lithium-ion battery negative electrodes with the benefits of being a recycled material with extremely low associated carbon/energy footprints and potentially low material cost.

Experimental

The samples characterized in this report are sourced by Resitec AS from three different PV monocrystalline wafer producers using the DWS process, identified as *kerf 1–3*. The samples were sourced in 2019, and from investigation of kerf from a large number of wafering factories, it is the honest opinion of Resitec AS that the chosen samples accurately represent the fundamental properties of DWS kerf as a general concept. As shown in the present article, SSA, particle size, and chemical purity varies somewhat depending on manufacturer processes, but the qualitative features such as morphology and crystallinity is an inherent feature of the DWS process. The as-received kerf samples are in the form of moist filter cake containing 20–60% water depending on the manufacturer. Samples treated in this paper are dried in-house at Resitec AS.

PSD was measured using a Malvern Mastersizer 2000 using water as the dispersant. The samples were deagglomerated by mortar and pestle before ultrasonicating a slurry of 0.5 g kerf in 100 ml water in a high intensity ultrasonic finger for 30 s.

BET[66] SSA of the samples was analyzed by N_2-gas physisorption at 77 K using ASAP2020 analyzer (Micromeritics®). ~0.3 g of sample was degassed at 80 °C under 100 μmHg for 1 h and at 150 °C under 100 mmHg for 7 h prior to gas adsorption/desorption analysis.

XRF and LECO analysis were conducted by Degerfors Laboratorium AB. XRF analysis was carried out on pre-dried samples pressed onto cellulose bases at 40 tons in a Thermo ARL 9900 in vacuum. Oxygen was analyzed in LECO TCH600 in a single-use graphite crucible, while Carbon is measured in either a LECO CS-444 or a CS-844. Glow discharge mass spectrometry (GDMS) was conducted by

Eurofins EAG Laboratories in Toulouse, France, according to their procedures.

XRPD data were collected with a Panalytical PRO MPD, using CuKα_1 radiation and a PIXcel detector. The samples were spread onto zero-background silicon discs. The 2θ range was 20–140°, the step length 0.013°, and the total measuring time 2 h.

Raman spectra were measured using a Labram HR 800 spectrometer with an 800 mm focal length spectrograph, using an air-cooled (~70 °C) and back-thinned CCD detector. Samples were excited using an air cooled double frequency Nd:YAG laser (532 nm) and at a laser power of ~0.5 mW. Spectra were collected with an exposure time of 5 s, accumulation number of 100, and using a 600 grooves/mm grating.

Simultaneous TG and DSC curves were recorded with a Netzsch Jupiter F3 STA up to 1100 °C. For runs in Ar atmosphere, oxygen in the atmosphere was reduced to a ppm level by the use of Netzsch's oxygen getter system. More sensitive TG measurements were also made with a TA Instruments Discovery thermo-balance and more sensitive DSC measurements with a Setaram SENSYS Evo instrument equipped with a Calvet 3D sensor on a ~23 mg sample. MS was performed with a Pfeiffer Thermostar instrument connected to the Discovery thermo-balance.

Solid-state magic-angle spinning (MAS) ^{29}Si NMR experiments were performed at the magnetic field strength $B_0 = 9.4$ T (^{29}Si Larmor frequency of 79.46 MHz) with Bruker Avance-III 400 spectrometer equipped with 7 mm probehead and using MAS rate $\nu_r = 7.00$ kHz. ^{29}Si MAS NMR acquisitions involved rotor-synchronized spin-echo sequence with p90°/p180° pulses of 5.25/10.50 μs, respectively, operated at the nutation frequency of 47 kHz. 256 signal transients with 600 s relaxation delay were collected. ^{1}H-^{29}Si cross-polarization (CPMAS) experiments employed ^{1}H p90° excitation pulse of 7 μs followed by Hartmann-Hahn matched radiofrequency fields applied for 2 ms contact interval and spinal64 proton decoupling at 40 kHz. 32768 signal transients with 2 s relaxation delay were collected. Chemical shifts were referenced with respect to neat tetramethylsilane at 0 ppm.

Field emission SEM analysis was performed on a Merlin, Carl Zeiss, Germany, with an acceleration voltage of 3 kV and a current of 100 pA.

The samples for XPS were prepared by pressing silicon powder into indium foil. Measurements were performed using a PHI Quantera II scanning XPS microprobe. Monochromatic Al Kα radiation (hν = 1486.7 eV) was used with a spot size of 100 μm and a photoelectron takeoff angle of 45°. The setup is regularly calibrated using reference samples of Ag, Au, and Cu according to the ISO standard 15472.[67] Charge was neutralized using a combination of low energy electrons and low energy Ar ions if/when X-ray exposure caused charging. Data analysis was performed in CasaXPS. Shirley backgrounds and Gaussian-Lorenztian (GL(30)) peaks shapes were used throughout the peak fitting. Energy calibration was performed in all cases on the adventitious hydrocarbon peak (C–C), set to 284.8 eV, the validity of which is verified by the consistent positioning of the Si 2p$_{3/2}$ peak at ~99 eV. Spin-orbit split components for Si 2p species were separated by 0.58 eV.[68] Quantification was performed by area integration for each element and application of the respective relative sensitive factors from Yeh and Lindau.[69]

Scanning TEM investigations were carried out on a Thermo Fischer Themis operated at 300 kV. A comparatively thin particle was scanned twice. First in nanobeam diffraction mode where the condenser system was optimized to yield parallel illumination for a fully convergent probe, allowing for the collection of a series of diffraction patterns with a convergence angle of ~0.5 mrad and a probe diameter of approximately 3 nm. The patterns were collected with probe current 10 pA on a OneView in-situ camera at 300 frames per second using custom written synchronization software. The second scan was performed under standard STEM conditions for spectroscopy with probe current 150 pA. A convergence angle of 21.4 mrad and a collection angle of 23 mrad were used to simultaneously acquire low-loss and core-loss electron energy loss spectroscopy (EELS) hyperspectral datacubes. EDX was also acquired during this scan using a SuperX EDX detector. Data processing was performed using py4DSTEM[54] and HyDF.[55,56]

To investigate the effect of crystallinity, a sample of kerf 1 was heated in air to 400 °C to remove organic impurities and further crystallized in Ar at 850 °C (10 °C/min), named kerf 1-850. Electrodes were prepared with 76% Si, 12% C45 and 12% CMC. The aqueous slurry with 20% solid content was prepared using a MM 400 mixer mill (Retsch) for 30 min at 30 Hz and cast on Cu foil. 13 mm diameter discs were cut and dried overnight under vacuum at 120 °C. The mass loadings were ~1.2 mg/cm^2 and 5 mg/cm^2 for electrochemical testing and operando and in situ XRPD analysis, respectively. Pouch half cells with lithium metal counter and reference electrodes used Celgard 2325 separator and 50 μL (80 μL for operando and in situ XRPD) electrolyte consisting of LP57 (BASF, 1 M $LiPF_6$ in ethylene carbonate/ethyl methyl carbonate 3 : 7 vol%) with 10 vol% fluoroethylene carbonate and 2 vol% vinylene carbonate.

Electrochemical tests were performed using a Digatron BTS 600, an Arbin BT-2043 battery testing system for in situ XRPD and a SP-240 potentiostat (Bio-Logic) for operando XRPD. The cell was rested for 24 h after assembly to ensure complete wetting of the thick electrodes. For low mass loading electrodes, the lithiation was done at C/20 (1 C = 3579 mA/g) until 10 mV vs. Li^+/Li and then constant voltage until C/40; the delithiation was carried out at C/20 until 1.5 V vs. Li^+/Li. For operando XRPD the procedure was the same but with lower current densities, at C/100 and constant voltage until C/200 for kerf 1-850 and for kerf 1 at C/150 until C/250. In the case of in situ XRPD, both samples were lithiated at C/150 and then under constant voltage until full theoretical capacity was achieved (3579 mA/g) and delithiated at C/150 followed by a constant voltage at 1.5 V vs. Li^+/Li until current was below 30 μA.

Operando XRPD measurements during electrochemical testing were carried out on a STOE STADI P diffractometer in transmission mode using a Ge monochromator with a single-wavelength Cu Kα1 radiation (45 kV, 40 mA). A Mythen 1 K strip detector was used with a stationary angular 2θ range of 18.87° and angular resolution of 0.015°. The data collection for operando experiments was 15 min per pattern and for in situ experiments 30 min per pattern. Data analysis can be found in the supporting information.

Supporting Information

The authors have cited additional references within supporting information.[70,71]

Acknowledgements

Authors thank Yu-Chuan Chien and Ashok S. Menon for their help with the operando XRPD experiments. Authors acknowledge the financial support from the COBRA project (Horizon 2020 grant agreement number 875568) and STandUP for Energy. The Myfab-LIMS facility at Uppsala University is

acknowledged for enabling the collection of the SEM images and XPS spectra.

Conflict of Interests

Resitec is a commercial supplier of recycled kerf based products.

Data Availability Statement

The data that support the findings of this study are available from the corresponding author upon reasonable request.

Keywords: amorphous materials · diamond wire sawing kerf · lithium-ion battery anode · secondary raw material · silicon

[1] Commission, "Communications from the Commission to the European Parliament, the Council, the European Economic and Social Committee and the Committee of the Regions: Closing the loop - An EU action plan for the Circular Economy, COM(2015) 614 final," can be found under https://eur-lex.europa.eu/legal-content/EN/TXT/?uri=CELEX:52015DC0614, **2015**.
[2] Commission, "Communications from the Commission to the European Parliament, the Council, the European Economic and Social Committee and the Committee of the Regions: A new circular economy action plan for a cleaner and more competitive Europe, COM(2020) 98 final," can be found under https://eur-lex.europa.eu/legal-content/EN/TXT/?uri=COM:2020:98:FIN, **2020**.
[3] K. Hachichi, A. Lami, H. Zemmouri, P. Cuellar, R. Soni, H. Ait-Amar, N. Drouiche, *Silicon* **2018**, *10*, 1579–1589.
[4] M. Vazquez-Pufleau, T. S. Chadha, G. Yablonsky, P. Biswas, *Sci. Rep.* **2017**, *7*, 40535.
[5] M. Dhamrin, T. Saitoh, K. Kamisako, in *25th Eur. Photovolt. Sol. Energy Conf. Exhib. 5th World Conf. Photovolt. Energy Convers.*, Valencia, Spain, **2010**.
[6] N. Drouiche, P. Cuellar, F. Kerkar, S. Medjahed, N. Boutouchent-Guerfi, M. Ould Hamou, *Renewable Sustainable Energy Rev.* **2014**, *32*, 936–943.
[7] K. Tomono, H. Furuya, S. Miyamoto, Y. Okamura, M. Sumimoto, Y. Sakata, R. Komatsu, M. Nakayama, *Sep. Purif. Technol.* **2013**, *103*, 109–113.
[8] K. Tomono, S. Miyamoto, T. Ogawa, H. Furuya, Y. Okamura, M. Yoshimoto, R. Komatsu, M. Nakayama, *Sep. Purif. Technol.* **2013**, *120*, 304–309.
[9] H. L. Yang, I. T. Liu, C. E. Liu, H. P. Hsu, C. W. Lan, *Waste Manage.* **2019**, *84*, 204–210.
[10] "EU ban on sale of new petrol and diesel cars from 2035 explained | News | European Parliament," can be found under http://www.europarl.europa.eu/news/en/headlines/economy/20221019STO44572/eu-ban-on-sale-of-new-petrol-and-diesel-cars-from-2035-explained, accessed May 3rd 2023, **2022**.
[11] *Roadmap on Advanced Materials for Batteries*, Directorate-General For Energy, Batteries Europe, European Technology And Innovation Platform, **2021**.
[12] H. Wu, L. Zheng, J. Zhan, N. Du, W. Liu, J. Ma, L. Su, L. Wang, *J. Power Sources* **2020**, *449*, 227513.
[13] T. Kasukabe, H. Nishihara, K. Kimura, T. Matsumoto, H. Kobayashi, M. Okai, T. Kyotani, *Sci. Rep.* **2017**, *7*, 42734.
[14] H.-G. Tan, J.-G. Duh, *J. Power Sources* **2016**, *335*, 146–154.
[15] N. P. Wagner, A. Tron, J. R. Tolchard, G. Noia, M. P. Bellmann, *J. Power Sources* **2019**, *414*, 486–494.
[16] L. Zhang, L. Zhang, J. Zhang, W. Hao, H. Zheng, *J. Mater. Chem. A* **2015**, *3*, 15432–15443.
[17] M. Maeda, K. Imamura, T. Matsumoto, H. Kobayashi, *Appl. Surf. Sci.* **2014**, *312*, 39–42.
[18] M. Vazquez-Pufleau, T. S. Chadha, G. Yablonsky, H. F. Erk, P. Biswas, *Ind. Eng. Chem. Res.* **2015**, *54*, 5914–5920.
[19] T. Saga, *NPG Asia Mater.* **2010**, *2*, 96–102.
[20] "LONGi N-type Mono Silicon Wafer," can be found under http://www.longi.com/en/products/silicon/n-type/, accessed April 26th, **2023**.
[21] "LONGi P-Type Mono Silicon Wafer," can be found under http://www.longi.com/en/products/silicon/p-type/, accessed April 26th, **2023**.
[22] "NorSun products," can be found under http://www.norsun.no/products, accessed April 26th, **2023**.
[23] M. A. Green, *Solar Cells: Operating Principles, Technology and System Applications*, Univ. Of New South Wales, Kensington, NSW, **1998**.
[24] N. E. Grant, P. P. Altermatt, T. Niewelt, R. Post, W. Kwapil, M. C. Schubert, J. D. Murphy, *Sol. RRL* **2021**, *5*, 2000754.
[25] "SDS_17240-01_V_1.02_CHEN", can be found under https://blaser-2022.neos-hosting.ch/sds-download/Switzerland-SDS_17240-01_V_1.02_CHEN.pdf, accessed April 26th, **2023**.
[26] "Safety data sheets – Blaser Swisslube | Our Liquid Tool. Your Success"., can be found under https://blaser.com/safety-data-sheets/, accessed April 26th 2023, **2021**.
[27] "SDS_17260-01_V_1.07_CHEN", can be found under https://blaser-2022.neos-hosting.ch/sds-download/Switzerland-SDS_17260-01_V_1.07_CHEN.pdf, accessed Arpil 26th, **2023**.
[28] "SDS_17270-02_V_1.01_CHEN", can be found under https://blaser-2022.neos-hosting.ch/sds-download/Switzerland-SDS_17270-02_V_1.01_CHEN.pdf, accessed Arpil 26th, **2023**.
[29] A. Kumar, S. N. Melkote, *Procedia Manuf.* **2018**, *21*, 549–566.
[30] F. Orapunt, L.-L. Tay, D. J. Lockwood, J.-M. Baribeau, M. Noël, J. C. Zwinkels, S. K. O'Leary, *J. Appl. Phys.* **2016**, *119*, 065702.
[31] N. C. Popa, D. Balzar, *J. Appl. Crystallogr.* **2002**, *35*, 338–346.
[32] M. Wojdyr, *J. Appl. Crystallogr.* **2010**, *43*, 1126–1128.
[33] A. T. Voutsas, M. K. Hatalis, J. Boyce, A. Chiang, *J. Appl. Phys.* **1995**, *78*, 6999–7006.
[34] S. V. Gaisler, O. I. Semenova, R. G. Sharafutdinov, B. A. Kolesov, *Phys. Solid State* **2004**, *46*, 1528–1532.
[35] D. M. Zhigunov, G. N. Kamaev, P. K. Kashkarov, V. A. Volodin, *Appl. Phys. Lett.* **2018**, *113*, 023101.
[36] G. E. Maciel, D. W. Sindorf, *J. Am. Chem. Soc.* **1980**, *102*, 7606–7607.
[37] I. S. Chuang, D. R. Kinney, C. E. Bronnimann, R. C. Zeigler, G. E. Maciel, *J. Phys. Chem.* **1992**, *96*, 4027–4034.
[38] I. S. Chuang, D. R. Kinney, G. E. Maciel, *J. Am. Chem. Soc.* **1993**, *115*, 8695–8705.
[39] S. Hayashi, K. Hayamizu, S. Yamasaki, A. Matsuda, K. Tanaka, *J. Appl. Phys.* **1986**, *60*, 1839–1841.
[40] M. K. Cheung, M. A. Petrich, *J. Appl. Phys.* **1993**, *73*, 3237–3241.
[41] X. Li, J. A. Gilbert, S. E. Trask, R. Uppuluri, S. H. Lapidus, S. Cora, N. Sa, Z. Yang, I. D. Bloom, F. Dogan, J. T. Vaughey, B. Key, *Chem. Mater.* **2021**, *33*, 4960–4970.
[42] P. Yogi, M. Tanwar, S. K. Saxena, S. Mishra, D. K. Pathak, A. Chaudhary, P. R. Sagdeo, R. Kumar, *Anal. Chem.* **2018**, *90*, 8123–8129.
[43] V. L. Deringer, N. Bernstein, A. P. Bartók, M. J. Cliffe, R. N. Kerber, L. E. Marbella, C. P. Grey, S. R. Elliott, G. Csányi, *J. Phys. Chem. Lett.* **2018**, *9*, 2879–2885.
[44] W.-L. Shao, J. Shinar, B. C. Gerstein, F. Li, J. S. Lannin, *Phys. Rev. B* **1990**, *41*, 9491–9494.
[45] A. Kumar, A. Kovalchenko, V. Pogue, E. Pashchenko, S. N. Melkote, *Procedia CIRP* **2016**, *45*, 147–150.
[46] A. Bidiville, K. Wasmer, R. Kraft, C. Ballif, *24th Eur. Photovolt. Sol. Energy Conf.* **2009**, *21–25 September 2009* .
[47] L. Rapp, B. Haberl, C. J. Pickard, J. E. Bradby, E. G. Gamaly, J. S. Williams, A. V. Rode, *Nat. Commun.* **2015**, *6*, 7555.
[48] E. B. Jones, V. Stevanović, *Phys. Rev. B* **2017**, *96*, 184101.
[49] M. Budnitzki, M. Kuna, *J. Mech. Phys. Solids* **2016**, *95*, 64–91.
[50] R. Gassilloud, C. Ballif, P. Gasser, G. Buerki, J. Michler, *Phys. Status Solidi A* **2005**, *202*, 2858–2869.
[51] K. Minowa, K. Sumino, *Phys. Rev. Lett.* **1992**, *69*.
[52] G. Weill, J. L. Mansot, G. Sagon, C. Carlone, J. M. Besson, *Semicond. Sci. Technol.* **1989**, *4*, 280–282.
[53] D. Ge, V. Domnich, Y. Gogotsi, *J. Appl. Phys.* **2003**, *93*, 2418–2423.
[54] B. H. Savitzky, S. E. Zeltmann, L. A. Hughes, H. G. Brown, S. Zhao, P. M. Pelz, T. C. Pekin, E. S. Barnard, J. Donohue, L. Rangel DaCosta, E. Kennedy, Y. Xie, M. T. Janish, M. M. Schneider, P. Herring, C. Gopal, A. Anapolsky, R. Dhall, K. C. Bustillo, P. Ercius, M. C. Scott, J. Ciston, A. M. Minor, C. Ophus, *Microsc. Microanal.* **2021**, *27*, 712–743.
[55] T. Thersleff, C.-W. Tai, *Microsc. Microanal.* **2023**, *29*, 166–179.
[56] T. Thersleff, S. Budnyk, L. Drangai, A. Slabon, *Ultramicroscopy* **2020**, *219*, 113116.

[57] T. Ohno, S. Tashiro, Y. Amano, N. Yoshida, R. Yoshida, H. Abe, *PLOS ONE* **2021**, *16*, e0245303.
[58] J. Hacaloğlu, I. Athar, L. Toppare, Y. Yağci, *J. Macromol. Sci. Part A* **2003**, *40*, 605–615.
[59] R. B. Bergmann, *Appl. Phys. Mater. Sci. Process.* **1999**, *69*, 187–194.
[60] F. Kail, J. Molera, J. Farjas, P. Roura, C. Secouard, P. Roca I Cabarrocas, *J. Phys. Condens. Matter* **2012**, *24*, 095401.
[61] A. Ulvestad, A. H. Reksten, H. F. Andersen, P. A. Carvalho, I. J. T. Jensen, M. U. Nagell, J. P. Mæhlen, M. Kirkengen, A. Y. Koposov, *ChemElectroChem* **2020**, *7*, 4349–4353.
[62] T. D. Hatchard, J. R. Dahn, *J. Electrochem. Soc.* **2004**, *151*, A838.
[63] J. Li, J. R. Dahn, *J. Electrochem. Soc.* **2007**, *154*, A156.
[64] W.-R. Liu, Z.-Z. Guo, W.-S. Young, D.-T. Shieh, H.-C. Wu, M.-H. Yang, N.-L. Wu, *J. Power Sources* **2005**, *140*, 139–144.
[65] D. Rehnlund, F. Lindgren, S. Böhme, T. Nordh, Y. Zou, J. Pettersson, U. Bexell, M. Boman, K. Edström, L. Nyholm, *Energy Environ. Sci.* **2017**, *10*, 1350–1357.
[66] S. Brunauer, P. H. Emmett, E. Teller, *J. Am. Chem. Soc.* **1938**, *60*, 309–319.
[67] M. P. Seah, *Surf. Interface Anal.* **2001**, *31*, 721–723.
[68] S. Dreiner, M. Schürmann, C. Westphal, H. Zacharias, *Phys. Rev. Lett.* **2001**, *86*, 4068–4071.
[69] J. J. Yeh, I. Lindau, *At. Data Nucl. Data Tables* **1985**, *32*, 1–155.
[70] J. Rodriguez-Carvajal, in *Abstr. Satell. Meet. Powder Diffr. XV Congr. IUCr*, Toulouse, France, **1990**, p. 127.
[71] A. V. Naumkin, A. Kraut-Vass, S. W. Gaarenstroom, C. Powell, **2012**, DOI 10.18434/T4T88K.

Manuscript received: July 13, 2023
Revised manuscript received: August 29, 2023
Version of record online: September 18, 2023